

RESEARCH ARTICLE

10.1029/2017JB015136

Key Points:

- Dynamic triggering explains aftershocks along the rupture plane, while static triggering explains the off-fault seismicity
- We find great spatial variability of the b values within the aftershock zone, suggesting strong heterogeneity in stress distribution and material
- We find no foreshock activity, which adds to a growing body of observations that intraplate earthquakes tend to not have foreshocks

Supporting Information:

- Supporting Information S1
- Data Set S1
- Data Set S2

Correspondence to:

X. Meng,
xiaofenm@usc.edu

Citation:

Meng, X., Yang, H., & Peng, Z. (2018). Foreshocks, b value map, and aftershock triggering for the 2011 M_w 5.7 Virginia earthquake. *Journal of Geophysical Research: Solid Earth*, 123. <https://doi.org/10.1029/2017JB015136>

Received 23 OCT 2017

Accepted 22 MAY 2018

Accepted article online 27 MAY 2018

Foreshocks, b Value Map, and Aftershock Triggering for the 2011 M_w 5.7 Virginia EarthquakeXiaofeng Meng^{1,2} , Hongfeng Yang³ , and Zhigang Peng⁴ 

¹Department of Earth and Space Sciences, University of Washington, Seattle, WA, USA, ²Now at Southern California Earthquake Center, University of Southern California, Los Angeles, CA, USA, ³Earth System Science Programme, The Chinese University of Hong Kong, Hong Kong, ⁴School of Earth and Atmospheric Sciences, Georgia Institute of Technology, Atlanta, GA, USA

Abstract The 2011 M_w 5.7 Virginia earthquake and subsequent dense deployment provide us an unprecedented opportunity to study in detail an earthquake sequence within stable continental United States. Here we apply the waveform-based matched filter technique to obtain more complete earthquake catalogs around the origin time of the Virginia mainshock. With the enhanced earthquake catalogs, we conclude that no foreshock activity existed prior to the Virginia mainshock. The b value map shows significant variations across the aftershock zone, suggesting strong heterogeneity in stress distribution or crustal material in the study region. We also investigate multiple earthquake triggering mechanisms, including static and dynamic triggering, afterslip, and atmospheric pressure changes. We find that dynamic triggering best explains aftershock distributions close to the mainshock's rupture plane, while the activation of off-fault seismicity is consistent with static Coulomb stress changes. Moreover, an off-fault earthquake swarm occurred as the Category 2 Hurricane Irene passed by the aftershock zone 5 days after the mainshock, which might be promoted by stress changes associated with atmospheric pressure drop. Our observations suggest that multiple mechanisms may be responsible for triggering aftershocks following one earthquake.

1. Introduction

On 23 August 2011 at 17:51:05, an moment magnitude (M_w) 5.7 earthquake struck Louisa County, Virginia (Figure 1). The mainshock ruptured a shallow, reverse fault striking N29°E and dipping 51° toward the south-east in the central Virginia seismic zone (CVSZ; Chapman, 2013). The CVSZ is an active intraplate seismic zone, where several moderate-size ($M \sim 5$) earthquakes occurred in the past (Bollinger, 1973; Kim & Chapman, 2005). Prior to the 2011 M_w 5.7 event, the latest moderate-size event in the CVSZ occurred on 9 December 2003 with a M_w of 4.3 (Kim & Chapman, 2005). The epicenters of the 2003 and 2011 events are only ~ 20 km apart. The 2011 Virginia mainshock had a complex rupture consisting of three subevents, which propagated from southwest at a depth of 8.0 km to northeast at depths of 7.3 and 7.0 km (Chapman, 2013). A very high stress drop of ~ 67 MPa for the mainshock was obtained (Q. Wu & Chapman, 2017). The high stress drop values are typical for intraplate regions, where earthquake recurrence times are much longer than interplate regions, and hence, the associated faults could be stronger due to longer-time fault healing processes (Allmann & Shearer, 2009; Kanamori & Anderson, 1975).

Prior to the Virginia mainshock, one broadband station CBN from the US network and six stations from the Virginia Tech Seismological Observatory (VTSO) were operating within 100 km (Figure 2a). However, the continuous data of VTSO stations was not archived till ~ 1.5 hr before the Virginia mainshock. To capture the aftershock sequence, 27 temporary seismic stations from four different networks were deployed around the epicenter between ~ 1.5 and 6 days following the mainshock (Chapman, 2013; McNamara et al., 2014). Because of the prompt and dense installation of seismic instruments, the detailed characteristics of this aftershock sequence have been well studied. In particular, 80 early aftershocks (up to 2 September 2011) are identified and located, using one temporary seismic network (Chapman, 2013). Three hundred eighty aftershocks are identified and located using four temporary networks from 25 August 2011 to 2 May 2012 by McNamara et al. (2014). Most aftershocks delineated a fault plane that was consistent with the focal mechanism of the mainshock (Box A in Figure 1). In addition, some aftershocks were northeast to the main cluster and shallower than 5 km (Box B in Figure 1). Q. Wu et al. (2015) performed aftershock detection with a combined method of Short-term-averaging/Long-term-averaging (STA/LTA) (Allen, 1982; Withers et al., 1998) and cross correlation. Then, they handpicked arrival times for the detected aftershocks and relocated 1,666 aftershocks with the hypoDD program (Waldhauser & Ellsworth, 2000).

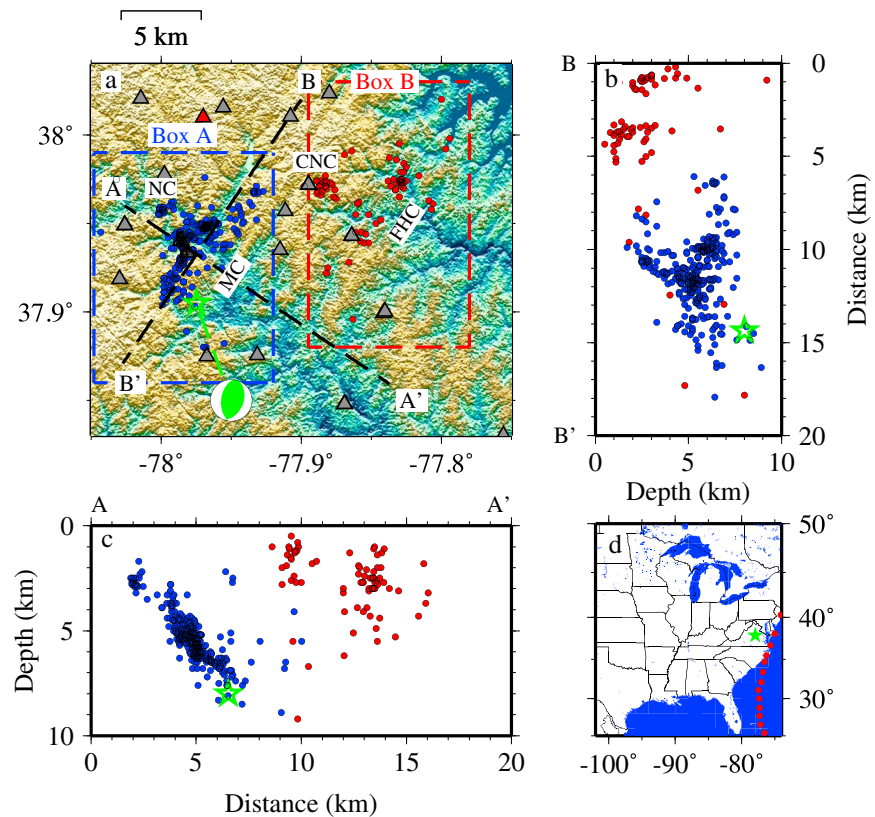


Figure 1. (a) Map view of the study region in Central Virginia. The background is topography. The green star and beachball denote the epicenter and focal mechanism of the Virginia mainshock, respectively. Blue and red dots denote templates in Boxes A and B, respectively. Grey triangles denote temporary seismic stations. The red triangle denotes the National Oceanic and Atmospheric Administration weather station. NC denotes Northwest Cluster. CNC denotes Cluster Northeast of Cuckoo. FHC denotes Fredericks Hall Cluster. (b) and (c) Cross-section view of study region along BB' and AA', respectively. (d) Map of Eastern United States. The green star denotes the epicenter of the Virginia mainshock. The red dots mark the track of Hurricane Irene.

Because of their infrequent occurrences, our understanding on the characteristics of intraplate earthquake sequences (e.g., *b* values, foreshock activity, and aftershock triggering) is quite limited. For example, how do the nucleation processes of intraplate earthquakes differ from interplate ones, as proposed by Bouchon et al. (2013)? It has been suggested that foreshocks provide crucial information on the nucleation process of large earthquakes (e.g., Ben-Zion, 2008; Dodge et al., 1995, 1996; Jones & Molnar, 1979), which may be a manifestation of slow slip that initiated the mainshock rupture (Dodge et al., 1995; McGuire et al., 2005). Alternatively, foreshocks simply trigger the subsequent mainshock in the same way as aftershock triggering (Felzer et al., 2004; Helmstetter et al., 2003). In addition, the degree of stress heterogeneity within an active intraplate seismic zone is not well known, which may be inferred by mapping *b* values. Finally, what physical mechanisms are most effective in triggering near-field aftershocks in intraplate regions? At plate boundary regions, different mechanisms (e.g., dynamic triggering, static triggering, and quasi-static triggering) have successfully explained the spatial pattern and/or temporal evolution of seismicity following certain mainshocks (Freed, 2005). However, different mechanisms are proposed to explain intraplate seismicity (e.g., Costain et al., 1987). In particular, Meng, Peng, Yang, and Allman (2013) found that the Virginia aftershock rate temporally increased during the Category 2 Hurricane Irene's passage, suggesting a possible triggering case. Answering these questions would significantly contribute to better seismic hazard assessment and mitigation in intraplate regions.

In this study, we obtain a complete earthquake sequence from 30 days before to 100 days after the Virginia mainshock by the matched filter technique (e.g., Meng, Peng, & Hardebeck, 2013; Peng & Zhao, 2009; Yang et al., 2009). We then examine the existence of foreshocks and its implication on the nucleation process.

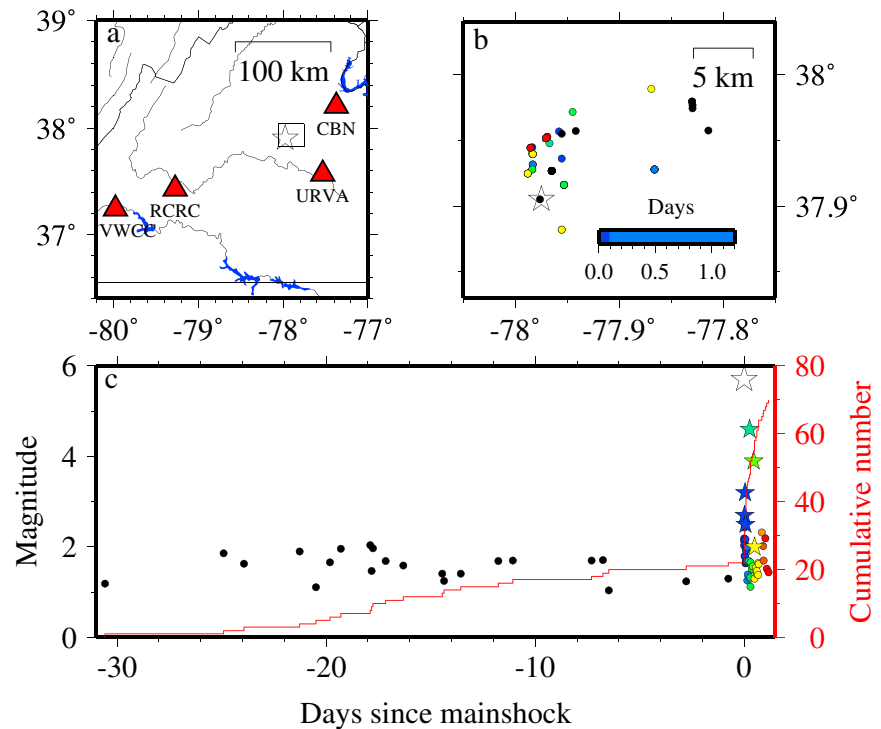


Figure 2. Detection results using regional permanent stations. (a) The star denotes the Virginia mainshock. Red triangles denote regional seismic stations. Black box denotes the plotting range of panel b. (b) A zoom-in plot showing the detected events before (black) and after (color coded) the mainshock, respectively. (c) Magnitude versus time for all detected events (dots) and templates (stars). The red line denotes the cumulative number of detected events.

Taking advantage of the massive amount of cross correlations done during aftershock detection at temporary stations, we obtain enhanced aftershock catalogs with carefully calibrated magnitudes and locations. The aftershock catalogs are then used to obtain detailed aftershock statistics and b value map. Finally, we investigate aftershock triggering following the Virginia earthquake (e.g., afterslip, static and dynamic triggering, and Hurricane Irene).

2. Data and Method

As mentioned before, the number of stations that have continuous recording changed significantly with time. Thus, we apply matched filter detections in three time windows separately using different configurations and data sets. The procedure follows that of Meng and Peng (2014) and is briefly described below.

2.1. Earthquake Detection Between 23 July 2011 at 00:00:00 and 23 August 2011 at 16:00:00

We perform single-station (i.e., CBN) earthquake detection between 23 July 2011 at 00:00:00 and 23 August 2011 at 16:00:00 (i.e., ~30 days before to ~1.5 hr before the mainshock). We use the 380 aftershocks from McNamara et al. (2014) as templates. The arrival times are predicted with a three-layer local velocity model (Chapman, 2013) in software COMLOC (Lin & Shearer, 2006). To improve the robustness of detection on a single station, we use both P and S waves signal windows (i.e., 1 s before to 4 s after the arrival) on three channels to cross correlate with the continuous data. We also require that each template must have at least three signal windows with signal-to-noise ratio larger than 5. Then, all correlation traces from one template are stacked to obtain the mean correlation trace. An event is detected when the mean correlation coefficient (CC) exceeds the sum of the median value and 9 times the median absolute deviation (MAD) of the mean correlation trace. We then remove all *duplicate detections* if their detecting time windows overlap. The hypocenter of the detected event is assigned to be the same with the best matching template following Peng and Zhao (2009). The magnitude of the detected event (M_{detected}) can be determined as

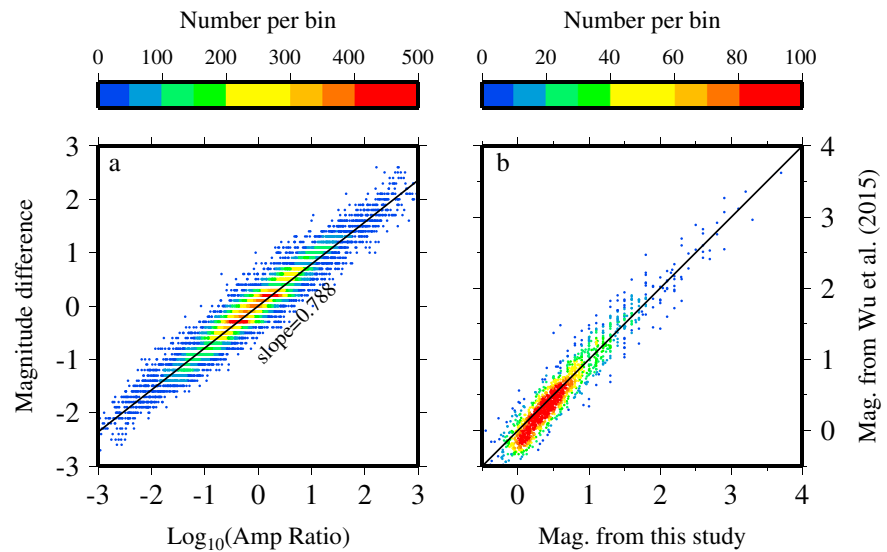


Figure 3. (a) Magnitude differences versus logarithmic amplitude ratio for all template pairs, color coded by their densities. The black line denotes the robust linear fit. (b) Magnitude comparison between this study and Q. Wu et al. (2015) for 1,469 events, color coded by density. The black line denotes one-to-one relationship.

$$M_{\text{detected}} = M_{\text{template}} + c \log_{10}(AR) \quad (1)$$

where M_{template} is the magnitude of the best matching template, AR is the amplitude ratio between the detected event and template, and c is the constant describing the scaling between magnitude and amplitude. Following most studies (e.g., Meng, Peng, & Hardebeck, 2013; Peng & Zhao, 2009; Schaff & Richards, 2014), we assign $c = 1.0$ for local magnitude, and AR is measured as the median peak amplitude ratio among all channels.

2.2. Earthquake Detection Between 23 August 2011 at 16:00:00 and 25 August 2011 at 00:00:00

Three VTSO stations within 150 km of the epicenter, together with station CBN, are used to detect the immediate foreshocks and aftershocks (i.e., ~1.5 hr before to ~30.5 hr after the mainshock; Figure 2a). The detection procedure is identical with that from section 2.1. An example of a newly detected early aftershock is shown in supporting information Figure S1.

2.3. Earthquake Detection, Magnitude Estimation, and Relocation Between 25 August 2011 at 00:00:00 and 1 December 2011 at 00:00:00

We apply a similar procedure to detect aftershocks using all temporary stations during this time window. The only difference in the matched filter setting is that we only use P and S waves on vertical and horizontal channels, respectively. Because the massive amount of cross correlations between newly detected events and templates are already done during the matched filter detection, we could take advantage of the waveform similarity information and perform magnitude estimation and relocation, following Shelly et al. (2016).

For magnitude estimation, we first calibrate c value from equation (1) using all templates from McNamara et al. (2014). We compare the amplitudes from two templates' waveforms (i.e., 5-s window around P or S wave arrival) on channels with high waveform similarity (i.e., >7 MAD) and compute the principal component slopes (Figure S2). The median slope among all channels is taken as AR between the two templates. After measuring AR for all template pairs, we perform the robust linear fit between magnitude differences and AR , and the best fitting slope is the calibrated c value (Figure 3a). Then, we compute the AR between each detected event and its best matching template in the same way and estimate M_{detected} using equation (1) with $c = 0.788$.

Similarly, as cross correlation between all pairs of earthquakes are already done, we can easily extract the correlation-derived differential traveltimes (i.e., dt_{cc}) from channels with high waveform similarity (supporting information text and Figure S3). The differential traveltimes are then used to precisely relocate all earthquakes in hypoDD.

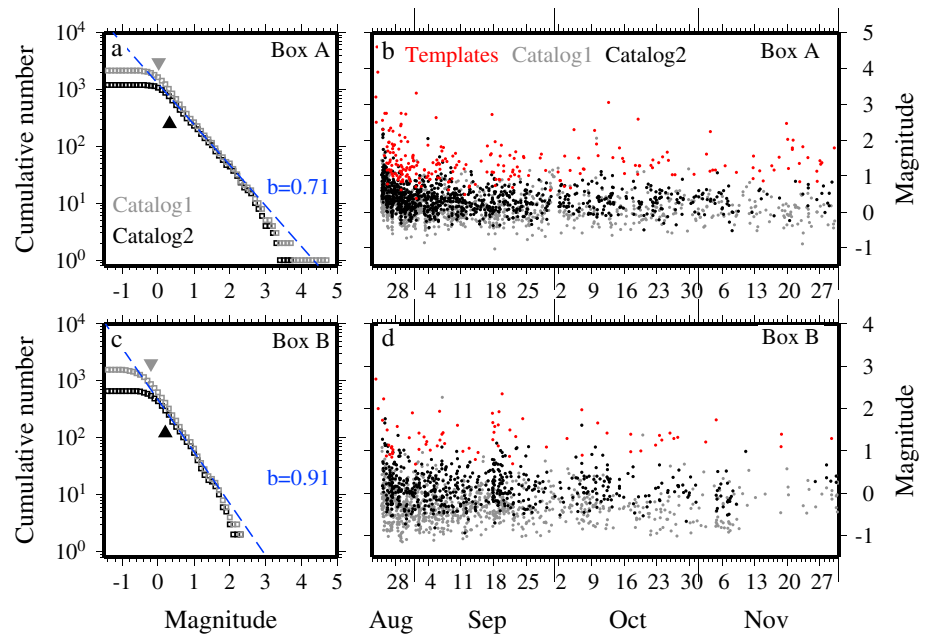


Figure 4. (a) Magnitude-frequency relationship for events in Box A from Catalog1 (grey squares) and Catalog2 (black squares). The grey and black triangles denote the M_c for Catalog1 and Catalog2, respectively. The blue dashed line denotes the best fitting Gutenberg-Richter relationship. (b) Magnitude versus origin time for the detected events in Catalog1 (grey), Catalog2 (black), and templates (red) in Box A. (c, d) The same plots for events in Box B.

3. Results

3.1. Detection of Foreshocks and Immediate Aftershocks

Within ~30 days prior to the Virginia mainshock, we detect 22 earthquakes with magnitude between 1.0 and 2.0 (Figure 2), none of which is listed in the Advanced National Seismic System (ANSS) Comprehensive Earthquake catalog. We do not detect any event within 1.5 hr before the mainshock with the addition of three VTSS stations. From the spectrogram, it is also evident that there was no high-frequency signal immediately before the mainshock (Figure S4). The seismicity rate leading up to the mainshock is stable, with no clear acceleration pattern.

Within ~30.5 hr after the mainshock, 47 aftershocks as small as $M_{1.1}$ are detected, which is an eightfold increase compared to the ANSS Comprehensive Earthquake catalog. Except for a few aftershocks within the first 500 s after the mainshock, all immediate aftershocks are successfully detected (Figure S4). Among the 47 early aftershocks, 39 and 8 events are in Boxes A and B, respectively. With the small number of early aftershocks, it is difficult to perform any additional statistical analysis or examine the spatiotemporal evolution.

3.2. Detection of Aftershocks With Temporary Stations

After matched filter detection and magnitude estimation, we obtain 3,800 aftershocks between 25 August 2011 and 1 December 2011, hereafter referred to as Catalog1 (Figure 4 and supporting information Data Set S1). Thanks to the dense temporary stations, we are able to recover aftershocks as small as magnitude -1 (Figure 4). Out of 1,666 events from Q. Wu et al. (2015) 1,469 are listed in Catalog1. The magnitude comparison between the two catalogs shows remarkable consistency across the entire magnitude range (Figure 3b). For events with $M < 0.5$, magnitudes from Catalog1 are slightly higher than that from Q. Wu et al. (2015).

After relocation with hypoDD, we obtain 1,859 earthquakes (hereafter referred to as Catalog2; Figures 4 and 5 and supporting information Data Set S2). As expected, the events that cannot be relocated are mostly aftershocks that did not occur close to other events or had very small magnitude (i.e., $M < 0.2$), because the low signal-to-noise ratio impedes measurements of dt_{cc} . The relocation results and corresponding errors are presented in Figures 5 and S5, respectively. The earthquakes in Box B have larger relocation errors than those in

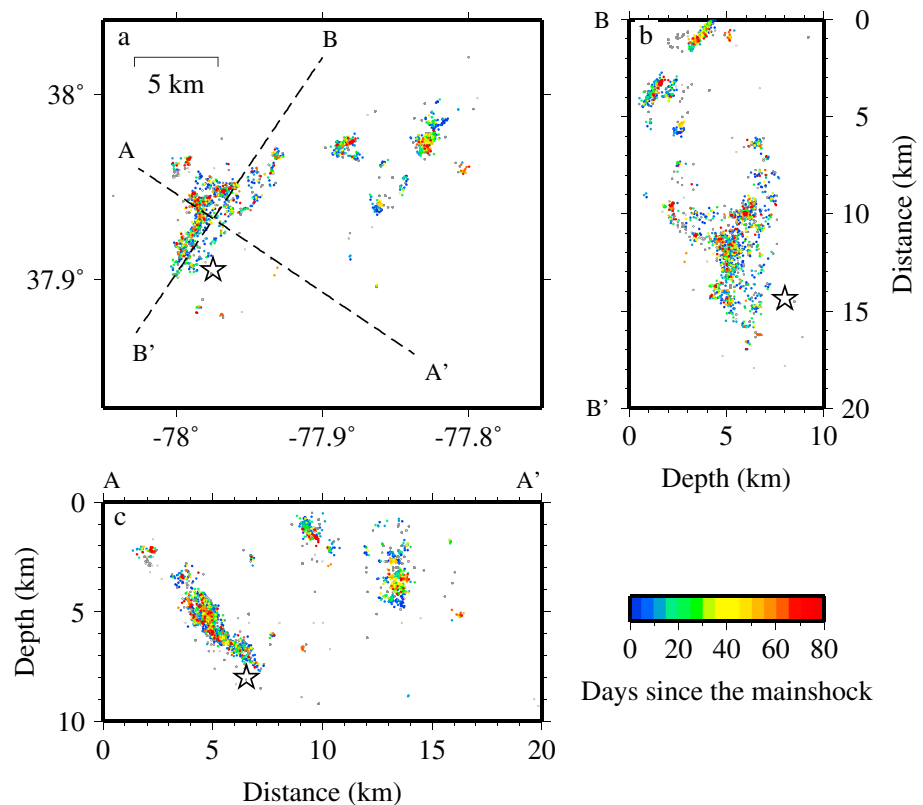


Figure 5. The hypoDD relocation results in (a) map and (b, c) cross-section view. The star denotes the Virginia mainshock. The grey dots denote template events. The relocated events are color coded by their origin times since the mainshock.

Box A (Figure S5), mainly because of worse network coverage and smaller number of clustered events. The relocated seismicity shows an almost identical pattern to that from Q. Wu et al. (2015; Figure 5). In Box A, majority of aftershocks depict a fault plane that strikes N34°E and dips 52° toward the southeast, and they are termed as the Main Cluster (MC). A cluster of shallow earthquakes was located northwest to the mainshock's rupture planes, which are termed as Northwest Cluster (NC). Horton et al. (2015) suggested that aftershocks in Box B can be further divided into two clusters: (1) a tight, shallow cluster of aftershocks (i.e., Cluster Northeast of Cuckoo or CNC) and (2) a cluster of aftershocks striking NE and dipping vertical (i.e., Fredericks Hall Cluster or FHC; Figure 1). However, our relocation results show that both clusters can be best characterized by fault planes striking NW and dipping NE (Figure 5). Moreover, focal mechanisms from these two clusters agree with a NNW striking fault plane (Q. Wu et al., 2015).

For the following analysis on aftershock statistics and temporal evolution, we focus primarily on Catalog1, as the large number of events significantly improves statistics and spatiotemporal resolution. Catalog2 is also examined in order to test the dependence of results on different catalogs. For the analysis on b value map, aftershock migration, and static Coulomb stress calculation, which requires well-constrained locations, we exclusively use Catalog2.

3.3. Statistical Behavior and b Value Map

Here we examine the statistical behaviors for both Catalog1 and Catalog2. In Box A, the magnitude of completeness (M_c) of Catalog1 and Catalog2 are 0.02 and 0.32, respectively, which are calculated by the best combined method in the software ZMAP (Wiemer, 2001; Figure 4a). The b value of both catalogs is ~ 0.91 , which is close to the global average (Okal & Sweet, 2007). In Box B, the M_c of Catalog1 and Catalog2 are -0.2 and 0.2 , respectively (Figure 4c). The b value, ~ 0.71 , is clearly lower than that in Box A. McNamara et al. (2014) and Q. Wu et al. (2015) calculated the b values of ~ 0.76 and ~ 0.86 , respectively, which are average values over two boxes.

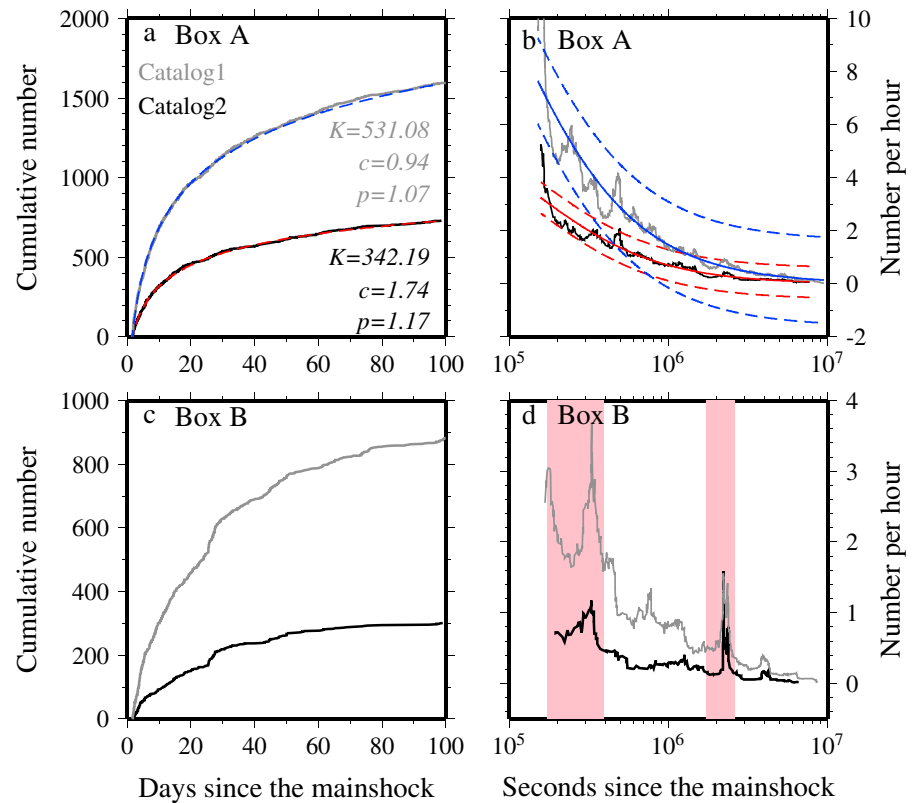


Figure 6. (a) The cumulative number of detected events above the M_c in Box A for Catalog1 (grey) and Catalog2 (black). The blue and red line denotes the best fitting Omori's law from software AFTPOI for Catalog1 and Catalog2, respectively. The best fitting parameters are labeled. (b) The seismicity rate decay in Box A for Catalog1 (grey) and Catalog2 (black). The blue solid and dashed lines denote the best fitting Omori's law and 2 times standard deviation for Catalog1. (c, d) The same plots for events in Box B. The pink shaded areas denote the time windows around two earthquake swarms.

In Box A, aftershocks above the M_c showed a typical Omori decay (Omori, 1894; Utsu et al., 1995) for both catalogs (Figures 6a and 6b). We fit the seismicity rate changes in Box A with the modified Omori's law using the software Aftpoi (Ogata, 2006). The best fitting p values for Catalog1 and Catalog2 are 1.07 and 1.17, respectively, which are close to that of a typical aftershock sequence (i.e., $p = 1$). Although the seismicity in Box B also gradually decayed with time (Figures 6c and 6d), the rate changes cannot be fitted by the modified Omori's law for either catalog, mainly because of two time periods with elevated seismicity rate (Figure 6d). A close examination reveals that the sudden increase in seismicity during the two time periods can be considered as earthquake swarms (Figure 7), which refer to sequences with the largest magnitude event not at the beginning of a sequence and similar magnitudes for all events (Mogi, 1962). We then apply the Epidemic Type Aftershock Sequence model to seismicity in Box B to further examine whether they are typical aftershock sequences (supporting information and Figure 8; Llenos et al., 2009; Ogata, 1988; Zhuang et al., 2002). As expected, the seismicity in both time periods showed significant deviations from the Epidemic Type Aftershock Sequence model, again suggesting that the two sequences are likely caused by stress transients or fluid migrations (e.g., Vidale & Shearer, 2006). However, we do not observe any systematic migration during the two swarms (Figures 7c and 7d), which is typically used to determine whether the sequence is driven by aseismic creep or fluid diffusion.

As shown in Figure 4, the overall b values in Boxes A and B are evidently different. To further quantify the spatial variation of b values, we compute the b value at each hypocenter with the nearest 100 events from Catalog2 (Figure 9). The b value map shows significant spatial variability across the study region. The majority areas in Box A have relatively low b values between 0.6 and 0.8, while the southwestern end of MC has much larger b values (i.e., > 1.0). In Box B, the b values of FHC are clearly larger than those in Box A, in the range of 0.8–1.0, and the CNC has the largest b values in the study region (> 1.2).

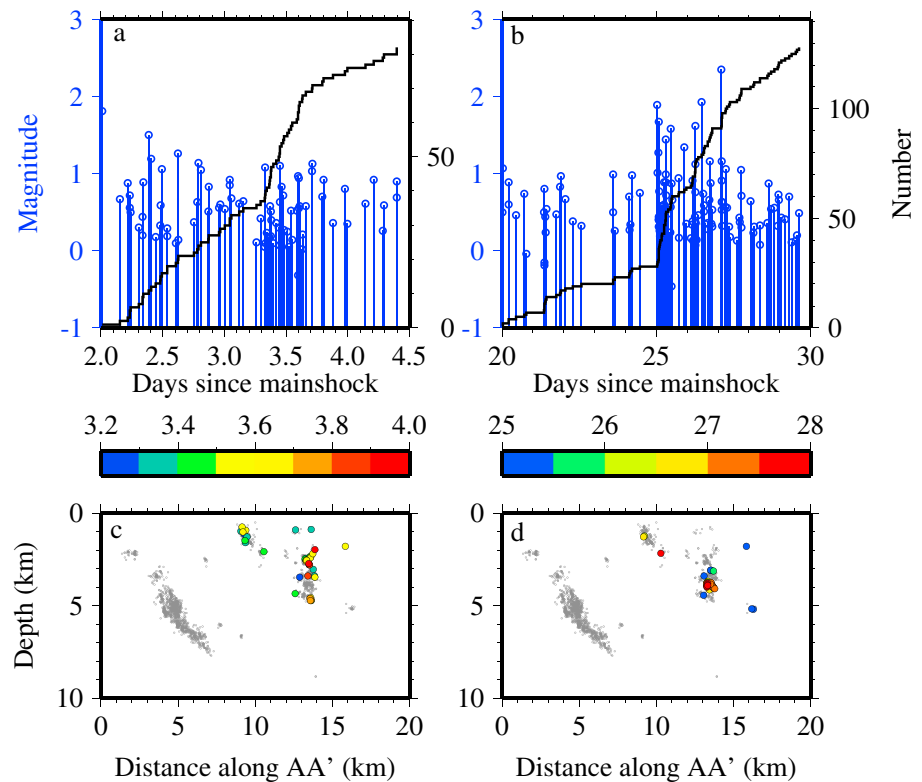


Figure 7. (a, b) Seismicity around the first and second earthquake swarms from Catalog2, respectively. The black line denotes the cumulative number of earthquakes. (c, d) The cross-section view of seismicity during the first and second swarms, respectively, which are color coded by the origin times since the mainshock. The grey dots denote all detected events.

4. Interpretations and Discussions

4.1. Comparison With Q. Wu et al. (2015)

The matched filter has become a new standard technique to complement local standard earthquake catalogs (e.g., Kato et al., 2012; Meng & Peng, 2016; Walter et al., 2015). Recently, Shelly et al. (2016) proposed a fully automated procedure for magnitude estimation and relocation following the matched filter detection. The procedure is efficient because it utilizes the massive amount of cross correlations performed during matched filter detection, especially for very large catalogs. Manually reviewing these newly detected events could be time consuming but still useful to evaluate the quality of the automatically detected catalog. For the 2011 Virginia earthquake, Q. Wu et al. (2015) published a well-constrained aftershock catalog using manually picked arrivals, which provides a useful data set for assessing the quality of the template matching catalog. Below we summarize the comparisons in magnitudes and locations for both catalogs.

Q. Wu et al. (2015) developed a new duration magnitude based on the regression between the standard duration magnitude and the distance-corrected peak amplitude for 100 large aftershocks. In this study, we estimate the extended local magnitude based on the amplitude ratio between the detected event and its best matching template. We find that magnitudes from two studies are mostly consistent (Figure 3b), suggesting that the automatic magnitude calibration is robust. We also find that for relatively small events (i.e., $M < 0.5$), the magnitude estimation in our catalog tends to be slightly higher. Such magnitude overestimation for small events may be caused by two factors. First, the scaling factor between local magnitude and amplitude ratio (i.e., $c = 0.788$) is computed from larger events. However, at small magnitudes, the measured amplitude ratio may scale linearly with seismic moment instead (e.g., Hanks & Boore, 1984; Shelly et al., 2016), which suggests that a better c value for small events is close to $2/3$. Second, we use a relatively long time window (i.e., 5 s) to compute the amplitude ratio between two events. For very small events, the coda

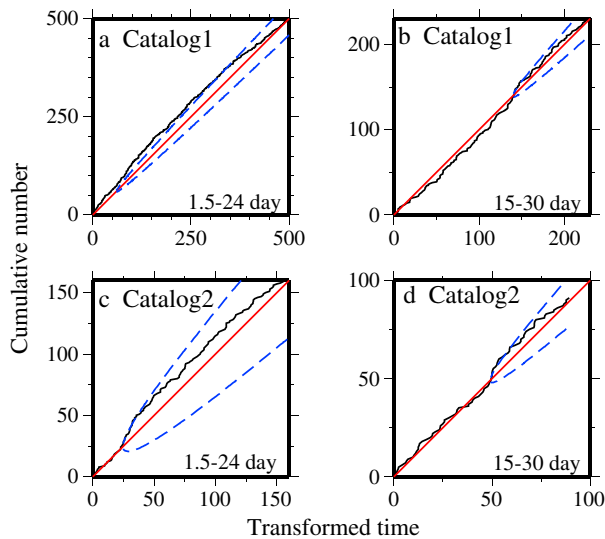


Figure 8. (a, b) ETAS modeling results for seismicity in Box B between 1.5 and 24 days and between 15 and 30 days after the mainshock, respectively. The black lines denote the observed seismicity rate. The red lines denote the seismicity rate predicted by ETAS. The blue dashed lines denote 2 times standard deviation. (c, d) The same plots for Catalog2. ETAS = Epidemic Type Aftershock Sequence.

wave amplitudes may become smaller than noises. Therefore, the usage of larger noise signals could overestimate the amplitude ratio and therefore local magnitude.

For hypoDD relocation, Q. Wu et al. (2015) used the differential travel-times derived from manually picked arrivals, while we exclusively use differential traveltimes from cross correlation (i.e., dt_{cc}). The primary motivation for using dt_{cc} is its efficiency, as no manual review is required and the computationally intensive cross correlation is already done in the template matching stage. Another potential benefit of dt_{cc} is that they result in smaller relative location error than manual picks (Waldhauser & Schaff, 2008). However, dt_{cc} measurements may suffer from cycle skipping or outliers. In this study, we applied two steps to reduce potential cycle skipping effects. First, only dt_{cc} associated with high CC (i.e., >7 MAD) is used, which is similar to the strategy used by Waldhauser and Schaff (2008) and Shelly et al. (2016). Furthermore, for the weighting function in hypoDD relocation, if the correlation trace has consecutive peaks with similar CC (e.g., possible sinusoid waveforms), its dt_{cc} measurement will have very small weight (see supporting information). In this way, we ensure that the reliable measurements dominate the weighting scheme. As a result, the number of relocated events in our catalog is slightly larger than that from Q. Wu et al. (2015), and the seismicity pattern is almost identical between the two studies. It is worth mentioning that some aftershocks isolated

from the seismicity clusters (e.g., MC, CNC, and FHC) in Q. Wu et al. (2015) do not exist in our catalog. This is due to the lack of enough neighboring events for isolated clusters.

4.2. Foreshock Activity

Some large earthquakes at plate boundaries are preceded by foreshocks, which are clearly elevated seismic activity compared to the background level (e.g., Kato et al., 2012; McGuire et al., 2005). Bouchon et al. (2013) found that large interplate earthquakes tend to have accelerating foreshock activity that may be driven by slow slip along the plate interface, while such phenomenon is much less common for intraplate earthquakes. One may argue that such conclusion is biased because intraplate regions tend to have poor seismic network coverage, where foreshocks are more likely missing from local catalogs with relatively high magnitude of completeness. Indeed, even for recent large interplate earthquakes, the accelerating and migrating foreshocks only showed up after matched filter detection (e.g., Kato et al., 2012; Kato & Nakagawa, 2014). Here we identified 22 earthquakes within 30 days before the 2011 Virginia mainshock with magnitude between 1.0 and 2.0. The seismicity rate prior to the Virginia mainshock does not show any acceleration pattern; instead, it appeared to slow down around ~ 10 days before the mainshock (Figure 2). The small magnitudes and stable occurrence rate suggest that these events are most likely background seismicity instead of foreshocks. Note that all templates used in detection are aftershocks. If foreshocks occurred along faults that are well separated from the aftershock zone and/or had significantly different focal mechanisms, they may remain undetected by our template library. Moreover, by visually examining the spectrogram ~ 1.5 hr before the mainshock (Figure S4), we confirm that no immediate foreshocks were observed. This observation adds to a growing body of evidences that no clear foreshock activity exists before moderate and large intraplate earthquakes (e.g., Doi & Kawakata, 2012; Ruan et al., 2017; C. Wu et al., 2014; Yang et al., 2009). However, there were also several mainshocks in eastern North American Plate preceded by foreshock activity, including several felt tremors days before the 1886 $M6.9-7.3$ Charleston earthquake (Dutton, 1889) and a $M4.7$ event 2 days before the 1988 $M5.9$ Saguenay, Quebec, earthquake (Somerville et al., 1990). These findings suggest that the nucleation process of intraplate earthquakes (and likely interplate earthquakes) is rather complicated, which requires careful earthquake identification and systematic studies for future events.

4.3. The b Value Map

It is commonly believed that b value from the Gutenberg-Richter relationship increases with decreasing differential stress level (Scholz, 1968). Schorlemmer et al. (2005) found that thrust-faulting events, which

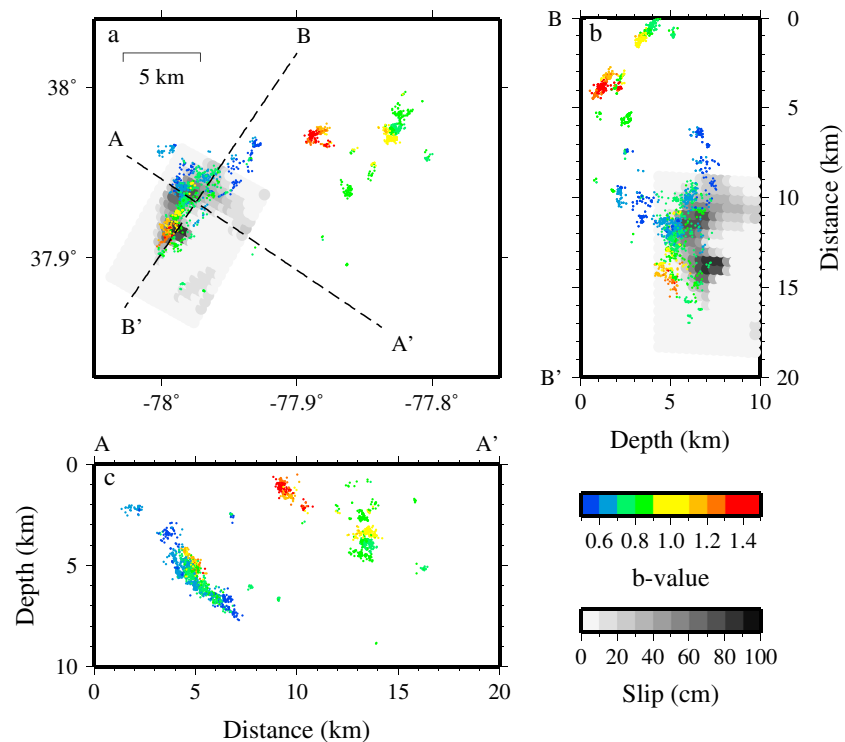


Figure 9. A comparison of the b value map obtained from Catalog2 and the finite slip model (Hartzell et al., 2013) in (a) map and (b, c) cross-section view. Each earthquake is color coded by the b value computed from 100 nearest neighbors.

are in higher stress regime, tend to have lower b values than normal faulting events, which are in lower stress regime. Moreover, there was a clear correlation between low b values obtained from earthquakes prior to the 2011 Tohoku-Oki earthquake and area with high slip during the mainshock, as well as increased b value after the mainshock and high slip (Tormann et al., 2015). For intraplate seismicity, the typical b value is around 0.8, lower than the global average of 1.0 (Okal & Sweet, 2007). The lower b value of intraplate earthquakes might indicate that intraplate faults are critically stressed due to a longer recurrence time.

The relatively large b values in Box B indicate relatively low differential stress level (Figure 9), which is consistent with the occurrences of two swarms possibly related to high fluid pressures. The low differential stress is also strongly supported by the stress drop studies by Q. Wu and Chapman (2017), in which they found very low stress drop (< 1 MPa) for aftershocks in Box B. The large b values at the southwestern end of MC are more complicated, as larger stress drop within MC suggests high differential stress level (Q. Wu & Chapman, 2017). Moreover, the seismicity at the southwestern end is located in areas with little slip during the mainshock (Hartzell et al., 2013) and marked the shallow limit of mainshock's slip (Q. Wu et al., 2015), which is opposite to the suggestion that large slip areas tend to have large b values (e.g., Tormann et al., 2015). Indeed, it has been pointed out that a large slip area may not be necessarily associated with high stress (Yin et al., 2016). Finally, the b values are also strongly affected by material and geometrical heterogeneity (Mogi, 1962). Areas with high material and geometrical heterogeneity are less likely to host large earthquakes (e.g., Yang et al., 2013), resulting in frequent smaller events and thus large b values. One example is the large b values at volcanoes due to high material heterogeneity near the magma chamber caused by the ascending magma (Wiemer & McNutt, 1997). The high material and geometrical heterogeneity at the southwest end of MC is supported by very diverse focal mechanisms, suggesting many minor faults with variable orientations (Q. Wu et al., 2015). In summary, the obtained spatial variability of the b values within the Virginia aftershock zone suggests that intraplate faults may have strong heterogeneity in stress distribution and material at local scale.

4.4. Aftershock Triggering Mechanisms

Below we explore possible mechanisms responsible for triggering aftershocks following the Virginia mainshock, including static and dynamic triggering, afterslip, and Hurricane Irene. Static and dynamic triggering

for this sequence have already been investigated by Q. Wu et al. (2015), but we include them here to complete the discussion.

4.4.1. Dynamic Versus Static Triggering

The two most important earthquake triggering mechanisms are the transient stress changes associated with radiated seismic waves (i.e., dynamic triggering) and permanent stress changes caused by fault displacement (i.e., static triggering). Although earthquakes triggered at remote distances can be only attributed to dynamic stresses, the debate on dynamic versus static triggering in the near field (i.e., within one or two rupture lengths), where dynamic and static stress changes are comparable, has been ongoing for the past decades (e.g., Felzer & Brodsky, 2006; Richards-Dinger et al., 2010). In the near field, dynamic triggering is difficult to observe, because the mainshock's wave train is short and the frequency contents of mainshocks' coda waves and triggered aftershocks are very similar. Moreover, the static Coulomb stress calculations in the near field are very sensitive to the slip model and receiving fault parameters (e.g., Zhan et al., 2011).

In Box A, as pointed out by Q. Wu et al. (2015), aftershocks located exclusively NE to the mainshock's epicenter (Figure 5), which is consistent with the rupture directivity (i.e., SW to NE). Such asymmetric aftershock distribution has often been used as evidence for near-field dynamic triggering due to the focusing of dynamic stresses (e.g., Gomberg et al., 2003; Kilb et al., 2002). Q. Wu et al. (2015) also resolved the static Coulomb stress changes on the nodal planes of known focal mechanisms using a source model based on the location and moment release of three subevents (Chapman, 2013) and found that ~80% of focal mechanisms in Box A are promoted closer to failure. However, as mentioned before, the static Coulomb stress calculations at such close distances within the rupture plane are extremely sensitive to the changes in the slip model, focal mechanism solutions, and aftershock locations and hence are subject to large uncertainties. In addition, for the temporal evolution of the aftershock sequence, the Omori's law decay in Box A can be explained by the rate- and state-dependent friction model with a stress step (Dieterich, 1994). On the other hand, Brodsky (2006) argued that dynamically triggered earthquake sequence could also follow Omori's law, as they may be secondary aftershocks of a large triggered event.

In Box B, the first two earthquakes occurred ~15 and ~35 min after the mainshock (Figure S4), with magnitude of 2.0 and 2.7, respectively. However, the long delay time does not completely eliminate the possibility of dynamic triggering. Delayed triggering is not rare and may be explained by secondary triggering mechanisms initiated by dynamic stresses, like clock advance (Gomberg, 2001), aseismic creep (Shelly et al., 2011), or fluid migration (Manga & Brodsky, 2006). Q. Wu et al. (2015) found that 63% of the focal mechanisms in Box B experienced positive static Coulomb stress changes. Here we compute the static Coulomb stress changes using focal mechanisms from Q. Wu et al. (2015) with updated hypocenters in Catalog2 and the slip models by Chapman (2013; MC model) and Hartzell et al. (2013; SH model). For both MC and SH models, at least 60% of events in Box B are brought closer to failure no matter which nodal plane is used (Figure 10). Thus, regardless of slip models and catalogs, our results (together with those from Q. Wu et al. (2015)) suggest that static Coulomb stress changes could explain ~60% of aftershock triggering in Box B.

The key evidence to differentiate dynamic and static triggering is the existence of *stress shadow*, where seismicity is stifled by negative Coulomb stress changes (Harris et al., 1995; Harris & Simpson, 1992; Toda et al., 2012). However, stress shadow is difficult to observe in intraplate regions, because they usually do not have the high background seismicity rate needed to show clear rate decrease. Therefore, we could not confidently reject either dynamic or static triggering following the Virginia mainshock. The asymmetric distribution of aftershocks in Box A favors dynamic triggering, while the static triggering is the preferred mechanism in Box B because it is consistent with the Coulomb stress increases.

4.4.2. Afterslip

Increasing number of studies on aftershock triggering following moderate-size earthquakes focus on afterslip (e.g., Kato & Obara, 2014; Peng & Zhao, 2009; J. Wu et al., 2017), which is continuous aseismic slip above or below the mainshock rupture zone to compensate the slip deficit (Marone, 1998). Afterslip following large earthquakes can be identified by geodetic measurements. However, because of the lack of geodetic instruments around the epicenter of the Virginia mainshock, afterslip could have occurred but went undetected (Roeloffs et al., 2015). Therefore, we investigate the migration of earthquakes following the mainshock using Catalog2, which is often considered as manifestation of aseismic creep or afterslip (e.g., Kato et al., 2012; Peng & Zhao, 2009). We examine the spatial-temporal evolution of all seismicity along AA', BB', and depth (Figure 11). In both boxes, we find that the aftershock zone did not expand with time along either

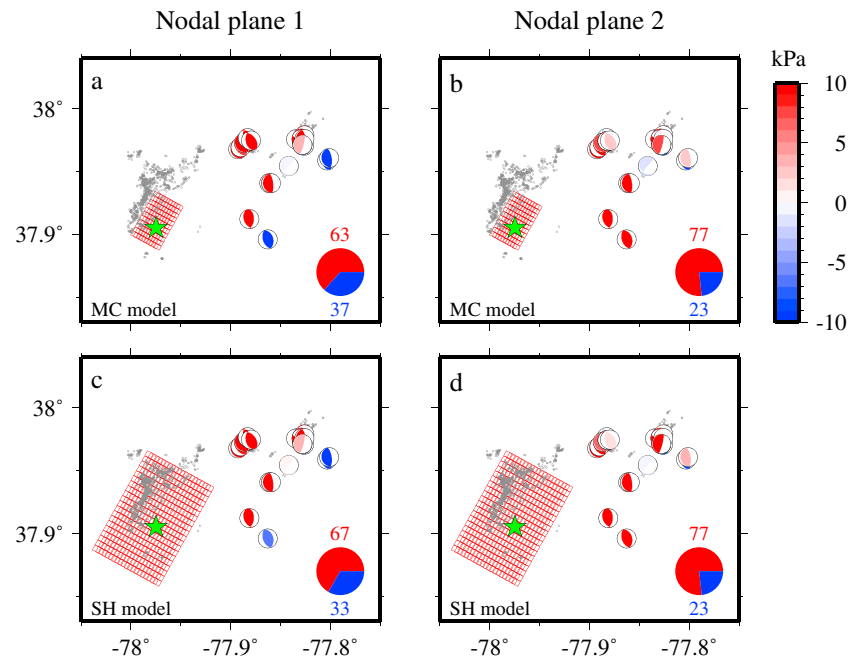


Figure 10. Static Coulomb stress changes using the MC (a, b) and SH models (c, d). Grey dots denote all detected earthquakes in Catalog2. Red grids denote the outline of slip models. Green star denotes the mainshock's epicenter from Chapman (2013). Focal mechanisms are from Q. Wu et al. (2015), which are color coded by static Coulomb stress changes. The pie chart denotes the percentage of positive and negative static Coulomb stress changes. MC model = slip model by Chapman (2013); SH model = slip model by Hartzell et al. (2013).

direction. We also identify six and seven repeater families (e.g., Nadeau et al., 1995; Peng & Ben-Zion, 2005; Peng & Zhao, 2009), which includes at least three events with highly similar waveforms (i.e., $CC > 0.9$), in Boxes A and B, respectively (Figure S6). Similarly, no migration of repeaters is observed (Figure 11). Therefore, along with the absence of geodetic measurements, we do not have any evidence for the existence of afterslip. In our case, the temporary seismic network were not deployed until ~ 30 hr after the mainshock. Hence, we cannot rule out the possibility that aftershock expansion occurred right after the mainshock but were not captured by the permanent stations.

4.4.3. Hurricane Irene

In critically stressed tectonic settings, seismic events may be prompted or inhibited by extreme weather events (e.g., rainfall, hurricane, or typhoon). For example, Hainzl et al. (2013) found that pore fluid pressure diffusion in subsurface due to rainfall-induced seismicity rate increase at Mount Hochstaufen, Germany. Seismicity modified by atmospheric pressure changes has also been studied but in much less extent. Gao et al. (2000) illustrated an annual modulation of the triggered earthquake rate in California following the 1992 M_w 7.3 Landers earthquake by atmosphere pressure changes, which reduce the normal stress along faults and enhance seismicity. Liu et al. (2009) suggested that some shallow slow-slip events were triggered along the Longitudinal Valley Fault in eastern Taiwan following several wet typhoons. However, a more recent study examining the same data set showed that most of the transient signals observed by borehole strain meters were associated with rainfalls, rather than aseismic slip at shallow depth (Hsu et al., 2015).

A few days following the Virginia mainshock, Hurricane Irene raked the East Coast of United States. Between Irene's two landfalls at Cape Lookout, North Carolina, and Brigantine Island, New Jersey, it passed through the aftershock zone of the Virginia mainshock with powerful swirls of wind (Avila & Cangialosi, 2011). The meteorological data (e.g., precipitation, temperature, and atmospheric pressure) is recorded every 20 min at the National Oceanic and Atmospheric Administration station 03715/LKU, ~ 10 km from the mainshock's epicenter (Figure 1a). We do not observe any significant changes in precipitation and temperature associated with Hurricane Irene (Figure S8). However, there was a clear atmospheric pressure drop between ~ 3 and ~ 5 days after the mainshock, which is caused by the pass-by of the hurricane eye center (Figure 12b). The onset of the first swarm in Box B coincided with the onset of the atmospheric pressure drop. Because the dominant

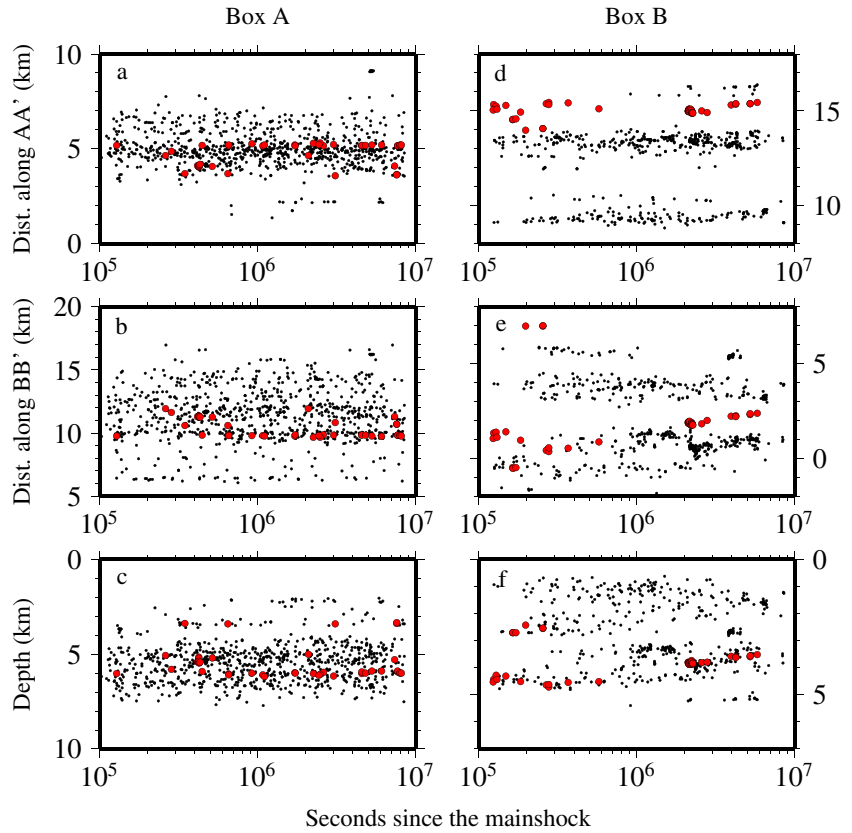


Figure 11. (a, d) Distance along AA' versus origin time for detected earthquakes (grey dots) and repeaters (red dots) in Boxes A and B, respectively. (b, e) Distance along BB' versus origin time. (c, f) Depth versus origin time.

faulting types in Box B are in reverse (Q. Wu et al., 2015), the seismicity rate increase during Hurricane Irene can be qualitatively explained by fault unclamping due to atmospheric pressure drop (Figure 12a), similar to how fluid extraction might change gravitational loading and induce earthquakes (Ellsworth, 2013).

To better quantify this, we predict the seismicity rate changes in Box B with the rate- and state-dependent friction model (Dieterich, 1994). We first compute the Coulomb stress rate on a reverse fault from atmospheric pressure changes (Figure 12b):

$$\dot{S}(t) = \dot{\sigma}(t) \sin(\theta) \cos(\theta) + \mu' \dot{\sigma}(t) \cos(\theta) \cos(\theta) (t > 0) \quad (2)$$

where $\dot{\sigma}(t)$ is atmospheric pressure rate (positive values denote atmospheric pressure decrease) computed from a sliding window of 20 data points, θ is the average dip angle among focal mechanisms in Box B (i.e., 50°), and μ' is effective friction coefficient (i.e., 0.4). Then, $\dot{S}(t)$ is interpolated with a time step of 0.001 day. At $t = 0$, we assume a 10 kPa Coulomb stress increase ΔS , which is the average static Coulomb stress change among 30 focal mechanisms in Box B, to generate a decaying aftershock sequence. Finally, we compute the seismicity rate $R(t)$ according to the rate- and state-dependent model (Dieterich, 1994):

$$R(t) = \frac{r}{\gamma \dot{S}} \quad (3)$$

where r is background seismicity rate, γ is state variable, and \dot{S} is background stress rate ($\gamma = \frac{1}{\dot{S}}$ at $t = 0$). For an arbitrary stress history, the evolution of $\gamma(t)$ can be computed as (Hainzl et al., 2013)

$$\gamma(t + dt) = \left(\gamma(t) + \frac{dt}{2A\sigma} \right) \exp\left(-\frac{\dot{S}(t)dt}{A\sigma} \right) + \frac{dt}{2A\sigma} \quad (4)$$

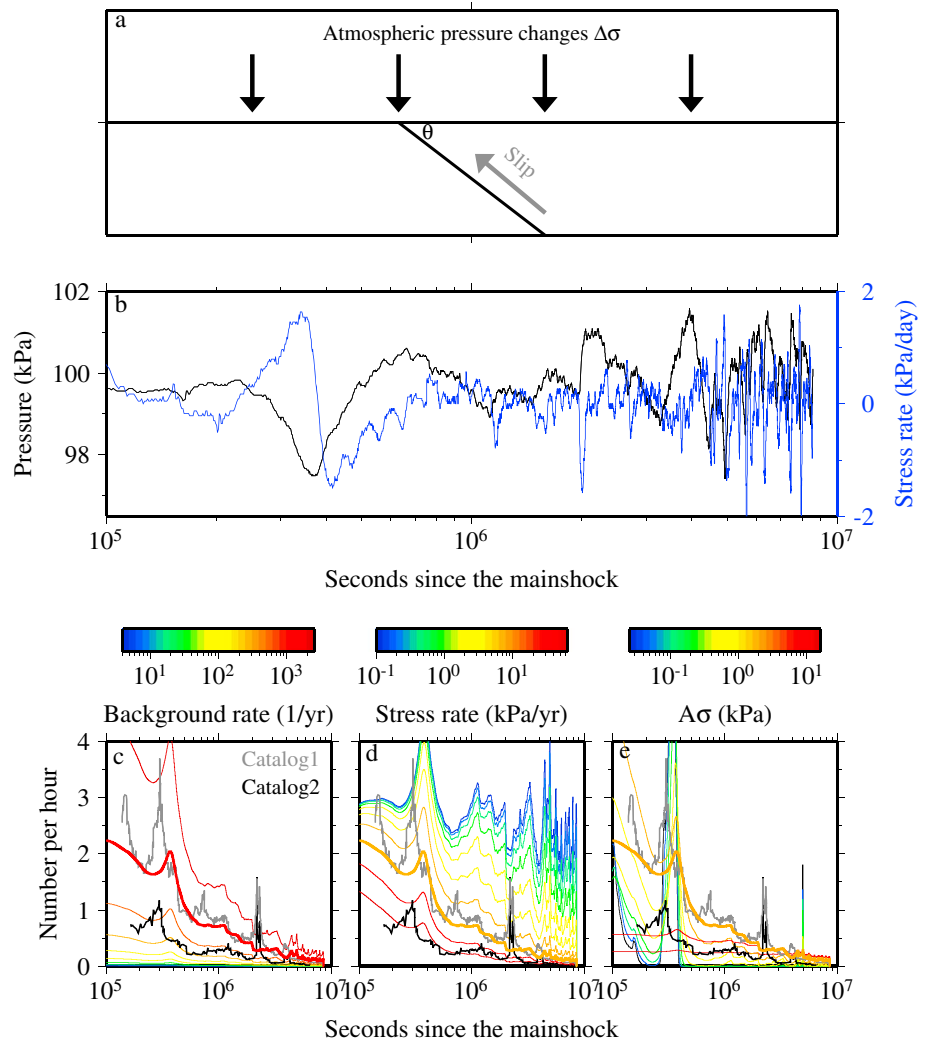


Figure 12. (a) A cartoon showing how atmospheric pressure changes $\Delta\sigma$ may affect reverse faulting with a dip angle θ . (b) Time series of atmospheric pressure and Coulomb stress rate acting on the reverse faulting plane. (c) The smoothed seismicity rate changes in Box B for Catalog1 (grey) and Catalog2 (black), and predicted seismicity rate changes with $\dot{S} = 12.8 \text{ kPa/year}$, $A\sigma = 3.2 \text{ kPa}$ and varying background seismicity rate r . The thick line denotes the optimized prediction. (d) Similar to panel (c), with $r = 1,024 \text{ year}^{-1}$, $A\sigma = 3.2 \text{ kPa}$, and varying stress rate \dot{S} . (e) Similar to panel (c), with $\dot{S} = 12.8 \text{ kPa/year}$, $r = 1,024 \text{ year}^{-1}$, and varying $A\sigma$.

where dt is sufficiently small time step (i.e., 0.001 day), σ is effective normal stress, A is a dimensionless fault constitutive friction parameter, and $\dot{S}(t)$ is the stress rate. \dot{S} , r , and $A\sigma$ are unknown parameters.

We predict the seismicity rate changes with a wide range of values for \dot{S} , r , and $A\sigma$ and compute the misfits with the observed seismicity rate in Box B during the entire study period (supporting information). The optimized parameter set is $\dot{S} = 12.8 \text{ kPa/year}$, $r = 1,024 \text{ year}^{-1}$, $A\sigma = 3.2 \text{ kPa}$. Both \dot{S} and $A\sigma$ are 1 order of magnitude larger than the optimized model parameters found by Hainzl et al. (2013) at Mount Hochstaufen, Germany, and smaller than typical interplate regions (e.g., Hainzl et al., 2009; Toda et al., 1998). The observed rate changes and optimized model prediction show very similar decay trend during the entire study period (Figure 12c). Moreover, the onsets of rate increase from the observed rate changes and optimized prediction during Hurricane Irene's pass-by are consistent. However, the optimized prediction has a smaller and more gradual rate increase, while the observed seismicity has a larger and steeper increase. The effects of varying parameters are illustrated in Figures 12c–12e. With higher r , lower \dot{S} , or lower $A\sigma$ values, the rate increase during Hurricane Irene's pass-by becomes larger and steeper, which is more similar with the observed data, but the misfits at other times become significantly larger.

We note that the above interpretation assumes that stress perturbations by Hurricane Irene cause the observed seismicity rate changes in Box B. In reality, aftershock activities fluctuate, especially at a short time-scales. Hence, while we do find some correlations between the atmospheric pressures and the seismicity rates, such correlation does not necessarily support a causal relationship between them. A more systematic study with a larger data set around the globe is needed to test the possible triggering relationship between hurricanes and earthquake occurrences (e.g., Wdowinski et al., 2017).

5. Conclusion

We perform single-station matched filter detection within 30 days before the 2011 Virginia earthquake and found no clear foreshock activity. With enhanced aftershock catalogs, we observe typical Omori's law decay for aftershocks close to the mainshock's rupture plane (Box A), while off-fault aftershock sequence (Box B) included two earthquake swarms. The b value map illustrates an overall lower b value in Box A than that in Box B. The significant spatial variability of b values suggests strong heterogeneity in stress distribution or crustal material in intraplate regions. Finally, we conduct a detailed investigation on aftershock triggering following the Virginia mainshock, including dynamic and static triggering, afterslip, and hurricane. No single triggering mechanism is able to explain all features in spatiotemporal distributions of aftershocks. The asymmetric aftershock distribution in Box A can be best explained by focusing of radiated dynamic stresses, while the static Coulomb stress changes better explain the triggering in Box B. Moreover, the first earthquake swarm in Box B may be related to the atmospheric pressure drop due to pass-by of Hurricane Irene. The results suggest that multiple triggering mechanisms contribute to aftershock triggering in intraplate regions, similar to previous studies at major plate boundaries (Daniel et al., 2008; Meng & Peng, 2014).

Acknowledgments

We thank Martin Chapman for providing VTSO data. All other seismic data used in this study are downloaded from IRIS Data Management Center. The earthquake catalogs used to generate figures are available as supporting information data sets. The manuscript benefits from useful discussions with Martin Chapman and Qiming Wu. X. M. and Z. P. are supported by USGS NEHRP grant G15AP00070 and NSF grants 1447091 and 1551022. H. Yang is supported by Faculty of Science at NSFC/RGC Joint Research Scheme (projects N_CUHK418/15 and N_CUHK430/16) and HKSAR Research Grant Council GRF grants 14313816 and 14305617. This work used the Extreme Science and Engineering Discovery Environment (XSEDE; Towns et al., 2014), which is supported by National Science Foundation grant ACI-1548562. This work used the Extreme Science and Engineering Discovery Environment (XSEDE) Stampede at the Texas Advanced Computing Center (TACC) through allocation TG-EAR140010. More detailed discussion of the methodology can be found in the supporting information (Ogata, 2006; Shelly et al., 2016).

References

- Allen, R. (1982). Automatic phase pickers—Their present use and future prospects. *Bulletin of the Seismological Society of America*, 72(6), S225–S242.
- Allmann, B. P., & Shearer, P. M. (2009). Global variations of stress drop for moderate to large earthquakes. *Journal of Geophysical Research*, 114, B01310. <https://doi.org/10.1029/2008JB005821>
- Avila, L. A., & Cangialosi, J. (2011). *Hurricane Irene, Trop. Cyclone Rep.*, (p. 44). Miami, FL: Natl. Hurricane Cent.
- Ben-Zion, Y. (2008). Collective behavior of earthquakes and faults: Continuum-discrete transitions, progressive evolutionary changes, and different dynamic regimes. *Reviews of Geophysics*, 46, RG4006. <https://doi.org/10.1029/2008RG000260>
- Bollinger, G. A. (1973). Seismicity of southeastern United States. *Bulletin of the Seismological Society of America*, 63(5), 1785–1808.
- Bouchon, M., Durand, V., Marsan, D., Karabulut, H., & Schmittbuhl, J. (2013). The long precursory phase of most large interplate earthquakes. *Nature Geoscience*, 6(4), 299–302.
- Brodsky, E. E. (2006). Long-range triggered earthquakes that continue after the wave train passes. *Geophysical Research Letters*, 33, L15313. <https://doi.org/10.1029/2006GL026605>
- Chapman, M. C. (2013). On the rupture process of the 23 August 2011 Virginia earthquake. *Bulletin of the Seismological Society of America*, 103(2A), 613–628.
- Costain, J. K., Bollinger, G. A., & Speer, J. A. (1987). Hydroseismicity—A hypothesis for the role of water in the generation of intraplate seismicity. *Geology*, 15(7), 618–621.
- Daniel, G., Marsan, D., & Bouchon, M. (2008). Earthquake triggering in southern Iceland following the June 2000 M_s 6.6 doublet. *Journal of Geophysical Research*, 113, B05310. <https://doi.org/10.1029/2007JB005107>
- Dieterich, J. (1994). A constitutive law for rate of earthquake production and its application to earthquake clustering. *Journal of Geophysical Research*, 99(B2), 2601–2618.
- Dodge, D. A., Beroza, G. C., & Ellsworth, W. (1996). Detailed observations of California foreshock sequences: Implications for the earthquake initiation process. *Journal of Geophysical Research*, 101, 22,371–22,392.
- Dodge, D. A., Beroza, G. C., & Ellsworth, W. L. (1995). Foreshock sequence of the 1992 Landers, California, earthquake and its implications for earthquake nucleation. *Journal of Geophysical Research*, 100(B6), 9865–9880.
- Doi, I., & Kawakata, H. (2012). A non-accelerating foreshock sequence followed by a short period of quiescence for a large inland earthquake. *Geophysical Research Letters*, 39, L11308. <https://doi.org/10.1029/2012GL051779>
- Dutton, C. E. (1889). The Charleston earthquake of August 31, 1886. *U.S. Geological Survey, Ninth Annual Report 1887-88*, 203–528.
- Ellsworth, W. L. (2013). Injection-induced earthquakes. *Science*, 341(6142), 142.
- Felzer, K., & Brodsky, E. (2006). Decay of aftershock density with distance indicates triggering by dynamic stress. *Nature*, 441(7094), 735–738.
- Felzer, K. R., Abercrombie, R. E., & Ekstrom, G. (2004). A common origin for aftershocks, foreshocks, and multiplets. *Bulletin of the Seismological Society of America*, 94(1), 88–98.
- Freed, A. M. (2005). Earthquake triggering by static, dynamic, and postseismic stress transfer. *Annual Review of Earth and Planetary Sciences*, 33, 335–367.
- Gao, S. S., Silver, P. G., Linde, A. T., & Sacks, I. S. (2000). Annual modulation of triggered seismicity following the 1992 Landers earthquake in California. *Nature*, 406(6795), 500–504.
- Gomberg, J. (2001). The failure of earthquake failure models. *Journal of Geophysical Research*, 106(B8), 16,253–16,263.
- Gomberg, J., Bodin, P., & Reasenber, P. (2003). Observing earthquakes triggered in the near field by dynamic deformations. *Bulletin of the Seismological Society of America*, 93(1), 118–138.
- Hainzl, S., Ben-Zion, Y., Cattania, C., & Wassermann, J. (2013). Testing atmospheric and tidal earthquake triggering at Mt. Hochstaufen, Germany. *Journal of Geophysical Research: Solid Earth*, 118, 5442–5452. <https://doi.org/10.1002/jgrb.50387>

- Hainzl, S., Enescu, B., Cocco, M., Woessner, J., Catalli, F., Wang, R., & Roth, F. (2009). Aftershock modeling based on uncertain stress calculations. *Journal of Geophysical Research*, *114*, B05309. <https://doi.org/10.1029/2008JB006011>
- Hanks, T. C., & Boore, D. M. (1984). Moment-magnitude relations in theory and practice. *Journal of Geophysical Research*, *89*(Nb7), 6229–6235.
- Harris, R., & Simpson, R. (1992). Changes in static stress on Southern California faults after the 1992 Lander earthquake. *Nature*, *360*(6401), 251–254.
- Harris, R., Simpson, R., & Reasenber, P. (1995). Influence of static stress changes on earthquake locations in Southern California. *Nature*, *375*(6528), 221–224.
- Hartzell, S., Mendoza, C., & Zeng, Y. H. (2013). Rupture model of the 2011 Mineral, Virginia, earthquake from teleseismic and regional waveforms. *Geophysical Research Letters*, *40*, 5665–5670. <https://doi.org/10.1002/2013GL057880>
- Helmstetter, A., Sornette, D., & Grasso, J. R. (2003). Mainshocks are aftershocks of conditional foreshocks: How do foreshock statistical properties emerge from aftershock laws. *Journal of Geophysical Research*, *108*(B1), 2046. <https://doi.org/10.1029/2002JB001991>
- Horton, J. W. Jr., Shah, A. K., McNamara, D. E., Snyder, S. L., & Carter, A. M. (2015). Aftershocks illuminate the 2011 Mineral, Virginia, earthquake causative fault zone and nearby active faults. *The Geological Society of America Special Papers*, *509*, 253–271.
- Hsu, Y. J., Chang, Y. S., Liu, C. C., Lee, H. M., Linde, A. T., Sacks, S. I., et al. (2015). Revisiting borehole strain, typhoons, and slow earthquakes using quantitative estimates of precipitation-induced strain changes. *Journal of Geophysical Research: Solid Earth*, *120*, 4556–4571. <https://doi.org/10.1002/2014JB011807>
- Jones, L. M., & Molnar, P. (1979). Some characteristics of foreshocks and their possible relationship to earthquake prediction and premonitory slip on faults. *Journal of Geophysical Research*, *84*(B7), 3596–3608.
- Kanamori, H., & Anderson, D. L. (1975). Theoretical basis of some empirical relations in seismology. *Bulletin of the Seismological Society of America*, *65*(5), 1073–1095.
- Kato, A., & Nakagawa, S. (2014). Multiple slow-slip events during a foreshock sequence of the 2014 Iquique, Chile M_w 8.1 earthquake. *Geophysical Research Letters*, *41*, 5420–5427. <https://doi.org/10.1002/2014GL061138>
- Kato, A., & Obara, K. (2014). Step-like migration of early aftershocks following the 2007 M_w 6.7 Noto-Hanto earthquake, Japan. *Geophysical Research Letters*, *41*, 3864–3869. <https://doi.org/10.1002/2014GL060427>
- Kato, A., Obara, K., Igarashi, T., Tsuruoka, H., Nakagawa, S., & Hirata, N. (2012). Propagation of slow slip leading up to the 2011 M_w 9.0 Tohoku-Oki earthquake. *Science*, *335*(6069), 705–708.
- Kilb, D., Gombert, J., & Bodin, P. (2002). Aftershock triggering by complete Coulomb stress changes. *Journal of Geophysical Research*, *107*(B4), 2060. <https://doi.org/10.1029/2001JB000202>
- Kim, W. Y., & Chapman, M. C. (2005). The 9 December 2003 central Virginia earthquake sequence: A compound earthquake in the central Virginia seismic zone. *Bulletin of the Seismological Society of America*, *95*(6), 2428–2445.
- Lin, G. Q., & Shearer, P. (2006). The COMLOC earthquake location package. *Seismological Research Letters*, *77*(4), 440–444.
- Liu, C., Linde, A., & Sacks, I. (2009). Slow earthquakes triggered by typhoons. *Nature*, *459*(7248), 833–836.
- Llenos, A. L., McGuiire, J. J., & Ogata, Y. (2009). Modeling seismic swarms triggered by aseismic transients. *Earth and Planetary Science Letters*, *281*(1–2), 59–69.
- Manga, M., & Brodsky, E. (2006). Seismic triggering of eruptions in the far field: Volcanoes and geysers. *Annual Review of Earth and Planetary Sciences*, *34*, 263–291.
- Marone, C. (1998). Laboratory-derived friction laws and their application to seismic faulting. *Annual Review of Earth and Planetary Sciences*, *26*, 643–696.
- McGuiire, J. J., Boettcher, M. S., & Jordan, T. H. (2005). Foreshock sequences and short-term earthquake predictability on East Pacific Rise transform faults. *Nature*, *434*(7032), 457–461.
- McNamara, D. E., Benz, H. M., Herrmann, R. B., Bergman, E. A., Earle, P., Meltzer, A., et al. (2014). The M_w 5.8 Mineral, Virginia, earthquake of August 2011 and aftershock sequence: Constraints on earthquake source parameters and fault geometry. *Bulletin of the Seismological Society of America*, *104*(1), 40–54.
- Meng, X., & Peng, Z. (2014). Seismicity rate changes in the Salton Sea Geothermal Field and the San Jacinto Fault Zone after the 2010 M_w 7.2 El Mayor-Cucapah earthquake. *Geophysical Journal International*, *197*(2), 1750–1762.
- Meng, X., & Peng, Z. (2016). Increasing lengths of aftershock zones with depths of moderate-size earthquakes on the San Jacinto Fault suggests triggering of deep creep in the middle crust. *Geophysical Journal International*, *204*(1), 250–261.
- Meng, X., Peng, Z., & Hardebeck, J. (2013). Seismicity around Parkfield correlates with static shear stress changes following the 2003 M_w 6.5 San Simeon earthquake. *Journal of Geophysical Research: Solid Earth*, *118*, 3576–3591. <https://doi.org/10.1002/jgrb.50271>
- Meng, X., Peng, Z., Yang, H., & Allman, S. (2013). Hurricane Irene's impacts on the aftershock sequence of the 2011 M_w 5.8 Virginia earthquake, in 2013 AGU fall meeting, San Francisco, CA.
- Mogi, K. (1962). Magnitude frequency relations for elastic shocks accompanying fractures of various materials and some related problems in earthquakes. *Bulletin. Earthquake Research Institute, University of Tokyo*, *40*, 831–853.
- Nadeau, R. M., Foxall, W., & Mcevilley, T. V. (1995). Clustering and periodic recurrence of microearthquakes on the San-Andreas Fault at Parkfield, California. *Science*, *267*(5197), 503–507.
- Ogata, Y. (1988). Statistical models for earthquake occurrences and residual analysis for point processes. *Journal of the American Statistical Association*, *83*(401), 9–27.
- Ogata, Y. (2006). Fortran programs statistical analysis of seismicity-updated version (point process data), EPTREN, LINLIN, SIMBVP, LINSIM and PGRAPH included in time series and control program package, SASeis2006, *Computer Science Monograph*, No. 33.
- Okal, E. A., & Sweet, J. R. (2007). Frequency-size distributions for intraplate earthquakes. *Continental Intraplate Earthquakes: Science, Hazard, and Policy Issues*, *425*, 59–71.
- Omori, F. (1894). On the aftershocks of earthquakes. *Journal of Colloid Science, Imperial University. Tokyo*, *7*, 111–200.
- Peng, Z., & Ben-Zion, Y. (2005). Spatiotemporal variations of crustal anisotropy from similar events in aftershocks of the 1999 $M7.4$ Izmit and $M7.1$ Duzce, Turkey, earthquake sequences. *Geophysical Journal International*, *160*(3), 1027–1043.
- Peng, Z., & Zhao, P. (2009). Migration of early aftershocks following the 2004 Parkfield earthquake. *Nature Geoscience*, *2*(12), 877–881.
- Richards-Dinger, K., Stein, R. S., & Toda, S. (2010). Decay of aftershock density with distance does not indicate triggering by dynamic stress. *Nature*, *467*(7315), 583–U105.
- Roeloffs, E., Nelms, D. L., & Sheets, R. A. (2015). Widespread groundwater-level offsets caused by the M_w 5.8 Mineral, Virginia, earthquake of 23 August 2011. *The Geological Society of America Special Papers*, *509*, 117–136.
- Ruan, X., Meng, X., Peng, Z., Long, F., & Xie, R. (2017). Microseismic activity in the last 5 months before the M_w 7.9 Wenchuan earthquake. *Bulletin of the Seismological Society of America*, *107*(4), 1582–1592.

- Schaff, D. P., & Richards, P. G. (2014). Improvements in magnitude precision, using the statistics of relative amplitudes measured by cross correlation. *Geophysical Journal International*, *197*(1), 335–350.
- Scholz, C. H. (1968). Frequency-magnitude relation of microfracturing in rock and its relation to earthquakes. *Bulletin of the Seismological Society of America*, *58*(1), 399.
- Schorlemmer, D., Wiemer, S., & Wyss, M. (2005). Variations in earthquake-size distribution across different stress regimes. *Nature*, *437*(7058), 539–542.
- Shelly, D. R., Ellsworth, W. L., & Hill, D. P. (2016). Fluid-faulting evolution in high definition: Connecting fault structure and frequency-magnitude variations during the 2014 Long Valley Caldera, California, earthquake swarm. *Journal of Geophysical Research: Solid Earth*, *121*, 1776–1795. <https://doi.org/10.1002/2015JB012719>
- Shelly, D. R., Peng, Z. G., Hill, D. P., & Aiken, C. (2011). Triggered creep as a possible mechanism for delayed dynamic triggering of tremor and earthquakes. *Nature Geoscience*, *4*(6), 384–388.
- Somerville, P. G., McLaren, J. P., Saikia, C. K., & Helmberger, D. V. (1990). The 25 November 1988 Saguenay, Quebec, earthquake—Source parameters and the attenuation of strong ground motion. *Bulletin of the Seismological Society of America*, *80*(5), 1118–1143.
- Toda, S., Stein, R. S., Beroza, G., & Marsan, D. (2012). Aftershocks halted by static stress shadows. *Nature Geoscience*, *5*(6), 410–413.
- Toda, S., Stein, R. S., Reasenberg, P. A., Dieterich, J. H., & Yoshida, A. (1998). Stress transferred by the 1995 $M_w = 6.9$ Kobe, Japan, shock: Effect on aftershocks and future earthquake probabilities. *Journal of Geophysical Research*, *103*(B10), 24,543–24,565.
- Tormann, T., Enescu, B., Woessner, J., & Wiemer, S. (2015). Randomness of megathrust earthquakes implied by rapid stress recovery after the Japan earthquake. *Nature Geoscience*, *8*(2), 152–158.
- Towns, J., Cockerill, T., Dahan, M., Foster, I., Gaither, K., Grimshaw, A., et al. (2014). XSEDE: accelerating scientific discovery. *Computing in Science & Engineering*, *16*(5), 62–74.
- Utsu, T., Ogata, Y., & Matsuura, R. (1995). The centenary of the Omori formula for a decay law of aftershock activity. *Journal of Physics of the Earth*, *43*(1), 1–33.
- Vidale, J. E., & Shearer, P. M. (2006). A survey of 71 earthquake bursts across Southern California: Exploring the role of pore fluid pressure fluctuations and aseismic slip as drivers. *Journal of Geophysical Research*, *111*, B05312. <https://doi.org/10.1029/2005JB004034>
- Waldhauser, F., & Ellsworth, W. (2000). A double-difference earthquake location algorithm: Method and application to the northern Hayward fault, California. *Bulletin of the Seismological Society of America*, *90*(6), 1353–1368.
- Waldhauser, F., & Schaff, D. P. (2008). Large-scale relocation of two decades of Northern California seismicity using cross-correlation and double-difference methods. *Journal of Geophysical Research*, *113*, B08311. <https://doi.org/10.1029/2007JB005479>
- Walter, J. I., Meng, X., Peng, Z., Schwartz, S. Y., Newman, A. V., & Protti, M. (2015). Far-field triggering of foreshocks near the nucleation zone of the 5 September 2012 ($M 7.6$) Nicoya Peninsula, Costa Rica earthquake. *Earth and Planetary Science Letters*, *431*, 75–86.
- Wdowinski, S., Peng, Z., Ferrier, K., Lin, C. H., Hsu, Y. J., & Shyu, J. B. H. (2017). Cascading hazards: Understanding triggering relations between wet tropical cyclones, landslides, and earthquakes. In *2017 AGU Fall meeting*. New Orleans, LA.
- Wiemer, S. (2001). A software package to analyze seismicity: ZMAP. *Seismological Research Letters*, *72*, 373–382.
- Wiemer, S., & McNutt, S. R. (1997). Variations in the frequency-magnitude distribution with depth in two volcanic areas: Mount St Helens, Washington, and Mt Spurr, Alaska. *Geophysical Research Letters*, *24*(2), 189–192.
- Withers, M., Aster, R., Young, C., Beiriger, J., Harris, M., Moore, S., & Trujillo, J. (1998). A comparison of select trigger algorithms for automated global seismic phase and event detection. *Bulletin of the Seismological Society of America*, *88*(1), 95–106.
- Wu, C., Meng, X., Peng, Z., & Ben-Zion, Y. (2014). Lack of spatiotemporal localization of foreshocks before the 1999 $M_w 7.1$ Duzce, Turkey, earthquake. *Bulletin of the Seismological Society of America*, *104*(1), 560–566.
- Wu, J., Yao, D. D., Meng, X. F., Peng, Z. G., Su, J. R., & Long, F. (2017). Spatial-temporal evolutions of early aftershocks following the 2013 $M_w 6.6$ Lushan earthquake in Sichuan, China. *Journal of Geophysical Research: Solid Earth*, *122*, 2873–2889. <https://doi.org/10.1002/2016JB013706>
- Wu, Q., & Chapman, M. (2017). Stress-drop estimates and source scaling of the 2011 Mineral, Virginia, mainshock and aftershocks. *Bulletin of the Seismological Society of America*, *107*(6), 2703–2720.
- Wu, Q., Chapman, M. C., & Beale, J. N. (2015). The aftershock sequence of the 2011 Mineral, Virginia, earthquake: Temporal and spatial distribution, focal mechanisms, regional stress, and the role of Coulomb stress transfer. *Bulletin of the Seismological Society of America*, *105*(5), 2521–2537.
- Yang, H., Liu, Y., & Lin, J. (2013). Geometrical effects of a subducted seamount on stopping megathrust ruptures. *Geophysical Research Letters*, *40*, 2011–2016. <https://doi.org/10.1002/grl.50509>
- Yang, H., Zhu, L. P., & Chu, R. S. (2009). Fault-plane determination of the 18 April 2008 Mount Carmel, Illinois, earthquake by detecting and relocating aftershocks. *Bulletin of the Seismological Society of America*, *99*(6), 3413–3420.
- Yin, J. X., Yang, H. F., Yao, H. J., & Weng, H. H. (2016). Coseismic radiation and stress drop during the 2015 $M_w 8.3$ Illapel, Chile megathrust earthquake. *Geophysical Research Letters*, *43*, 1520–1528. <https://doi.org/10.1002/2015GL067381>
- Zhan, Z. W., Jin, B. K., Wei, S. J., & Graves, R. W. (2011). Coulomb stress change sensitivity due to variability in mainshock source models and receiving fault parameters: A case study of the 2010–2011 Christchurch, New Zealand, earthquakes. *Seismological Research Letters*, *82*(6), 800–814.
- Zhuang, J., Ogata, Y., & Vere-Jones, D. (2002). Stochastic declustering of space-time earthquake occurrences. *Journal of the American Statistical Association*, *97*(458), 369–380.